Local photochemical nanoscopy of hot carrier−driven catalytic reactions using plasmonic nanosystems

Journal:	*ACS Nano*
Manuscript ID	Draft
Manuscript Type:	Article
Date Submitted by the Author:	n/a
Complete List of Authors:	Henrotte, Olivier; Palacky University Olomouc Santiago, Eva Yazmin; Ohio University, Physics and Astronomy Movsesyan, Artur; Ohio University, Department of Physics and Astronomy Mascaretti, Luca; Univerzita Palackeho v Olomouci, Regional Centre of Advanced Technologies and Materials Afshar, Morteza; Palacky University Olomouc Minguzzi, Alessandro; Universita degli Studi di Milano, Physical-Chemistry and Electrochemistry VERTOVA, ALBERTO; Universita degli Studi di Milano, Dipartimento di Chimica Wang, Zhiming; University of Electronic Science and Technology of China, Zbořil, Radek; Univerzita Palackeho v Olomouci, Regional Centre of Advanced Technologies and Materials, Department of Physical Chemistry Kment, Stepan ; Palacky University Olomouc, RCPTM, Palacky University Olomouc Govorov, Alexander; Ohio University, Physics and Astonomy Naldoni, Alberto; University of Turin, Department of Chemistry

Local photochemical nanoscopy of hot carrier–driven catalytic reactions using plasmonic nanosystems

Olivier Henrotte*, Eva Yazmin Santiago, Artur Movsesyan, Luca Mascaretti, Morteza Afshar, Alessandro Minguzzi, Alberto Vertova, Zhiming Wang, Radek Zbořil, Štěpán Kment, Alexander O. Govorov and Alberto Naldoni*

Keywords: photocatalysis; plasmonic; scanning electrochemical microscopy; in situ nanoscopy; hot charge carriers

Abstract

Nanoscale investigation on the reactivity of photocatalytic systems is crucial for their fundamental understanding and improving their design and applicability. Here, we present a photochemical nanoscopy technique that unlocks the local spatial detection of molecular products during plasmonic hot-carrier-driven photocatalytic reactions with nanometric precision. By applying the methodology to Au/TiO_2 plasmonic photocatalysts we experimentally and theoretically determine that smaller and denser Au nanoparticle arrays present lower absorption, but higher internal quantum efficiency in hot hole–driven photocatalysis. The highest quantum yield from the redox probe oxidation is achieved at the plasmon peak, whereas d–holes drive complex reactions such as water and chlorine oxidations with higher efficiency. Investigating a single plasmonic nanodiode we unravel the areas where oxidation and reduction products are evolved with sub–wavelength resolution. These results open the way to quantitative

investigations at the nanoscale to evaluate the photocatalytic reactivity of low–dimensional materials in a variety of chemical reactions.

Introduction

Chemical reactions driven by plasmonic nanomaterials have raised interest due to their increased selectivity[1] and mild condition requirements[2]. Upon light illumination, the collective oscillations of free carriers at the surface of conducting materials (i.e., surface plasmons) produce very intense electric fields localized in nanoscale volumes. Surface plasmons decay by generating non–equilibrium energetic electron−hole pairs (non-thermal or hot carriers), which have been shown to trigger photocatalytic reactions[3] by activating unusual pathways that impart enhanced product selectivity. The subsequent thermalization of the remaining carriers results in local heating, which also modifies the chemical reaction rate[4,5]. Plasmonic nanostructures offer superior absorption cross section in comparison with traditional photocatalysts such as molecular dyes and quantum dots[6]. Their optical properties depend on the composition, size, shape and media embedding the metallic nanostructures[7–10], thus enabling a vast playground for tuning their photocatalytic response[11]. Despite the increasing interest in developing plasmonic photocatalysts, photocatalytic efficiency are still very low (~0.1%[12]) due to the open challenges in understanding interfacial plasmon−driven reactions at the nanoscale[13].

The nanoscale mapping of plasmon–driven chemical reactions is a promising path to investigate the relationship between the intrinsic optical phenomena from plasmons and the consequent chemical reactivity[14–23]. Using optically−coupled in situ environmental transmission electron microscopy (TEM), Sytwu et al. have shown that plasmons in Au−PdH_x antenna−reactor systems activate catalytic sites on the nanorod lateral facets which, in dark conditions, are energetically−unfavorable in comparison to the usually reactive nanorod tips[16]. Cortés et al. used hot electron−driven self−assembly of nanoparticles (NPs) to show that plasmonic chemistry spatially localize on the corners of bowtie antennas, overlapping with electromagnetic hot

spots[17]. Similarly, Hamans et al. applied super−resolution fluorescence microscopy on single plasmonic nanorods demonstrating a spatial correlation between the plasmonic near field distribution and the plasmonic−driven fluorescence activation[18]. Other techniques, such as single NP absorption spectroscopy and electrochemical microscopy, can provide a glimpse about the reactivity of isolated nanostructures, which may differ from the behavior of ensemble systems, yet not offering information with spatial resolution[19–23]. These findings have revealed the strength of investigating the nanomaterial/molecule interactions at the nanoscale to elucidate the richness of reactivity offered by plasmon−driven photocatalysis. However, available mapping techniques so far are limited to TEM and spectroscopic methods. A scanning technique enabling the *in–situ* nanoscale mapping of photocatalytic chemical products evolved during plasmon–driven reactions is still missing.

Herein, we present a photochemical nanoscopy technique that enables the two−dimensional mapping of plasmonic reaction products, and thus of the hot carriers driving photocatalysis, with subwavelength resolution. This kind of approach open a new dimension in the understanding of the plasmonic reactivity by providing a direct correlation between materials properties and morphology with the energetics and the kinetics of the investigated chemical transformation.

Results and discussion

Mapping plasmonic photocatalysis over Au NP arrays on planar TiO_2

Our approach is based on investigating the morphological, optical and photochemical properties by a unique set of different scanning microscopy techniques, namely, scanning electron microscopy (SEM) (Figure1a,b), scanning spectrophotometer microscopy (SSM) (Figure 1a,c) and scanning photo-electrochemical microscopy (SPECM) (Figure 1a,d-f), at the same spatial point within plasmonic Au/TiO_2 photocatalysts. By adopting a model plasmonic system made by

Au NP arrays grown on a planar TiO_2 layer deposited over a charge collector (*i.e.*, indium tin oxide, ITO) support (Figure 1a), we unlocked the study of the reactivity of a specific type of charge carriers generated upon illumination (*i.e.*, hot holes[21]) by increasing their otherwise ultra-short lifetimes (~10-40 fs)[5,24–26]. The charge separation and molecular detection mechanisms are the following (Figure 1g): (1) upon visible light excitation, hot carriers are generated in the Au NPs, (2) the hot electrons with energy above the Schottky barrier (ϕ_B) are injected into the TiO_2 conduction band (CB), while the corresponding hot holes accumulate in the Au NPs. (3) These hot holes may oxidize the molecular species present in the electrolyte, provided that their energy is lower (higher oxidizing power) than the HOMO level of the molecules in solution. (4) The oxidized species diffuse toward an ultra−micro electrode (UME) where they are detected[27]. In this study, we used the ferrocene dimethanol, $Fc(MeOH)_2$, a redox mediator characterized by an outer−sphere one electron transfer mechanism, which ensures that the surface adsorption step during the catalytic reaction is negligible. Since the HOMO level of $Fc(MeOH)_2$ is close to the Au/TiO_2 Fermi level (E_F) in our system[21,28], the rate of photo-oxidized molecules can be considered as the maximum number of hot holes reacting per unit of time.

SPECM served as in-situ detection technique to measure the local concentration evolution of molecular species in solution under steady−state regime generated from the plasmonic photocatalysts. Plasmonic hot holes generated from such systems have been previously quantified using the redox competition (RC) mode (Figure 1d)[21], during which a competition happens for the same reaction between the active material and the UME[29]. Here, we adopted an alternative approach named substrate generation – tip collection (SG−TC) mode (Figure 1d): the oxidation reaction occurs at the substrate, while the UME electrochemically reduces back the oxidized species produced by the substrate. The SG−TC mode ensures higher signal sensitivity

and stability as the initial concentration of the produced species is near–zero, which corresponds to a near-zero dark current (Figure 1d). Scanning the photocatalyst surface while measuring the UME current under dark and light conditions (Figure 1e) allows to plot the differential current ($\Delta I = I_{light}$-I_{dark}) as photoactivity maps (Figure 1f).

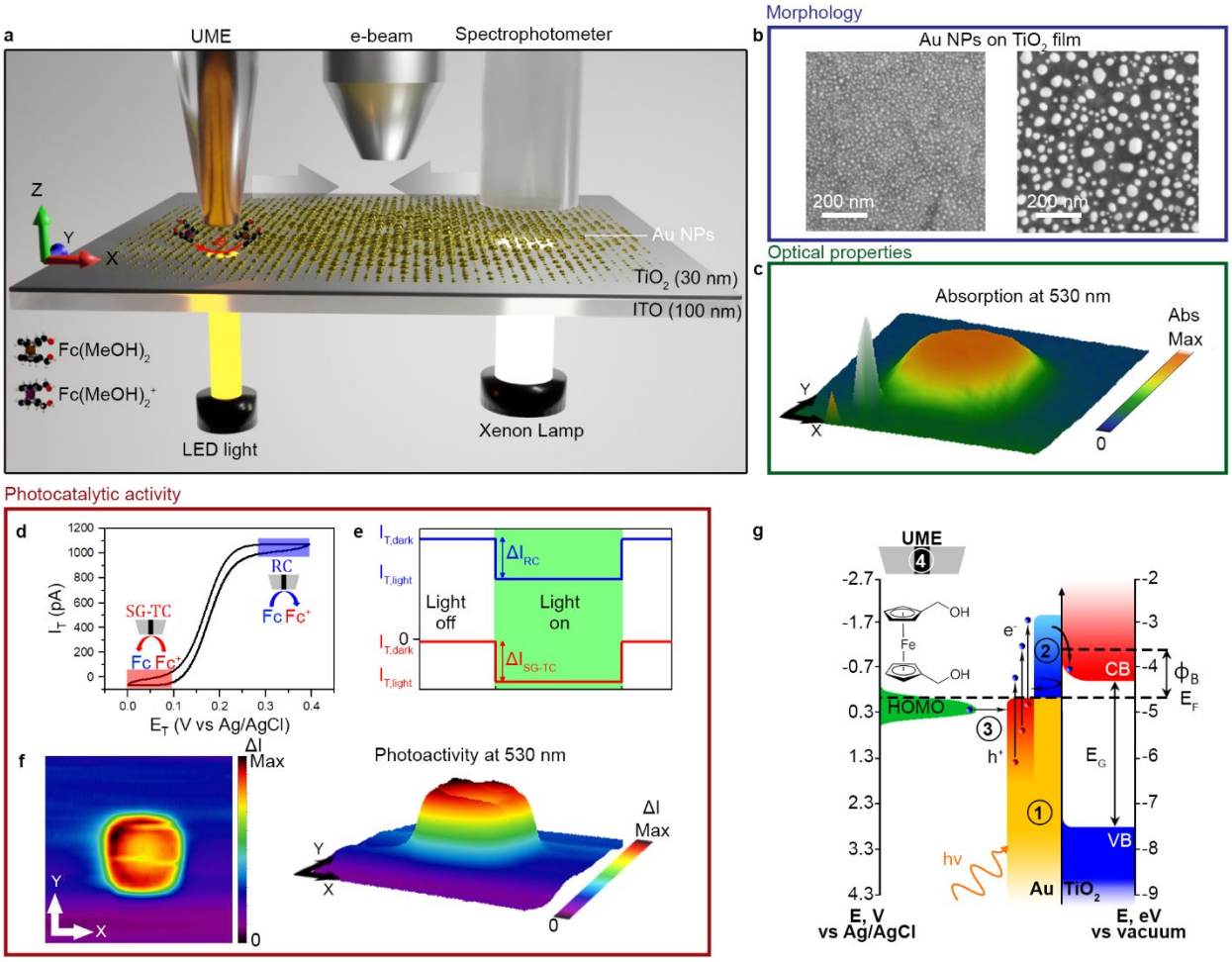

Figure 1. 2D mapping of the morphological, optical and photochemical properties of plasmonic Au/TiO_2 photocatalysts. a, Representation depicting the scanning techniques used to investigate the morphological, optical and photochemical properties of plasmonic planar Au/TiO_2 systems. **b**, SEM images of Au NPs deposited on planar TiO_2 films. **c**, 2D map of the absorption at 530 nm of the planar Au/TiO_2. **d**, Cyclic voltammetry representing two different

potential windows where steady-state is reached for SG-TC (red square) and RC (blue square) detection modes. **e**, Fixed position photoactivity measurement for SG-TC (red line) and RC (blue line) modes. **f**, SPECM 2D map of the photoactivity at 530 nm of the planar Au/TiO_2. **g**, Illustration of the principles underlying the plasmonic reactivity quantification in planar Au/TiO_2 photocatalysts.

Mapping plasmonic photocatalysis over Au NP arrays on planar TiO_2

To validate our methodology, we investigated first the Au NP arrays grown on a planar TiO_2/ITO substrate due to its well-known plasmonic and photochemical properties[12,20,21,24,30–35]. The Au/TiO_2/ITO films were fabricated by sputtering 10 nm thick Au film onto a 30 nm layer of TiO_2 deposited on ITO using atomic layer deposition (see Methods). Au was sputtered through a mask patterned with 256 squares of 100 μm side and spaced by 400 μm (Figure S1) that can be investigated during one SPECM experiment, thus providing instantaneous feedback on the validity of the collected data. After thermal dewetting at 400°C, Au truncated nanospheres with various size were formed inside the squares (Figure S2-S4). The controlled size of the squares forced the formation of a gradient in the Au NPs size distribution from the edge to the center (Figure S5-S8). The areas numbered 1 to 7 within a representative Au square (Figure 2a) are spaced by 20 μm and correspond to the positions where high magnification SEM images were performed to determine the Au NPs size distribution (Figure 2b and S5). The mean diameter of the Au NPs increased monotonically from the edge (11 nm) to the center (27 nm) of the square, while accordingly their spatial density decreased from 2463 to 431 particles/μm² (Figure 2c and S5, Table S1).

The absorption spectra mapping highlighted that the localized surface plasmon resonance (LSPR) shifted depending on the position within a single square (Figure 2d). The experimental

data were compared with calculated absorption spectra (see Methods) obtained for various Au NPs size corresponding to the experimental data taken at different position in Square A (Figure S9, Table S2). The experimental (extracted from Figure S10) and theoretical absorption spectra at different positions (Figure 2e and S11) showed a good agreement in the LSPR shapes. As expected, we observed an increased plasmonic absorption from the edge to the center of the square due to the increase in the mean Au NPs diameter (<d>)[36,37]. Notably, our approach enabled also to visualize light absorption at fixed wavelengths while varying the position within the square (Figure 2f). These plots highlighted that: (i) the highest absorption was observed at 580 nm, which corresponds to the LSPR position; (ii) all the traces showed a steady increase in absorption through the square except for the curve obtained at 660 nm that showed a steep increase at the center of the square; (iii) theoretical absorption curves were in excellent agreement with experimental ones, especially in the spectral region overlapping with the LSPR. The slight shift (~20 nm) between experimental and computed spectra (Figure 2e) and difference in line scan trend (Figure 2f) might be related to the Au NPs heterogeneous population along the square (Figure S12). The less pronounced experimental absorption at λ<500 nm if compared to theoretical curves could be due to instrumental limitation in this energy range.

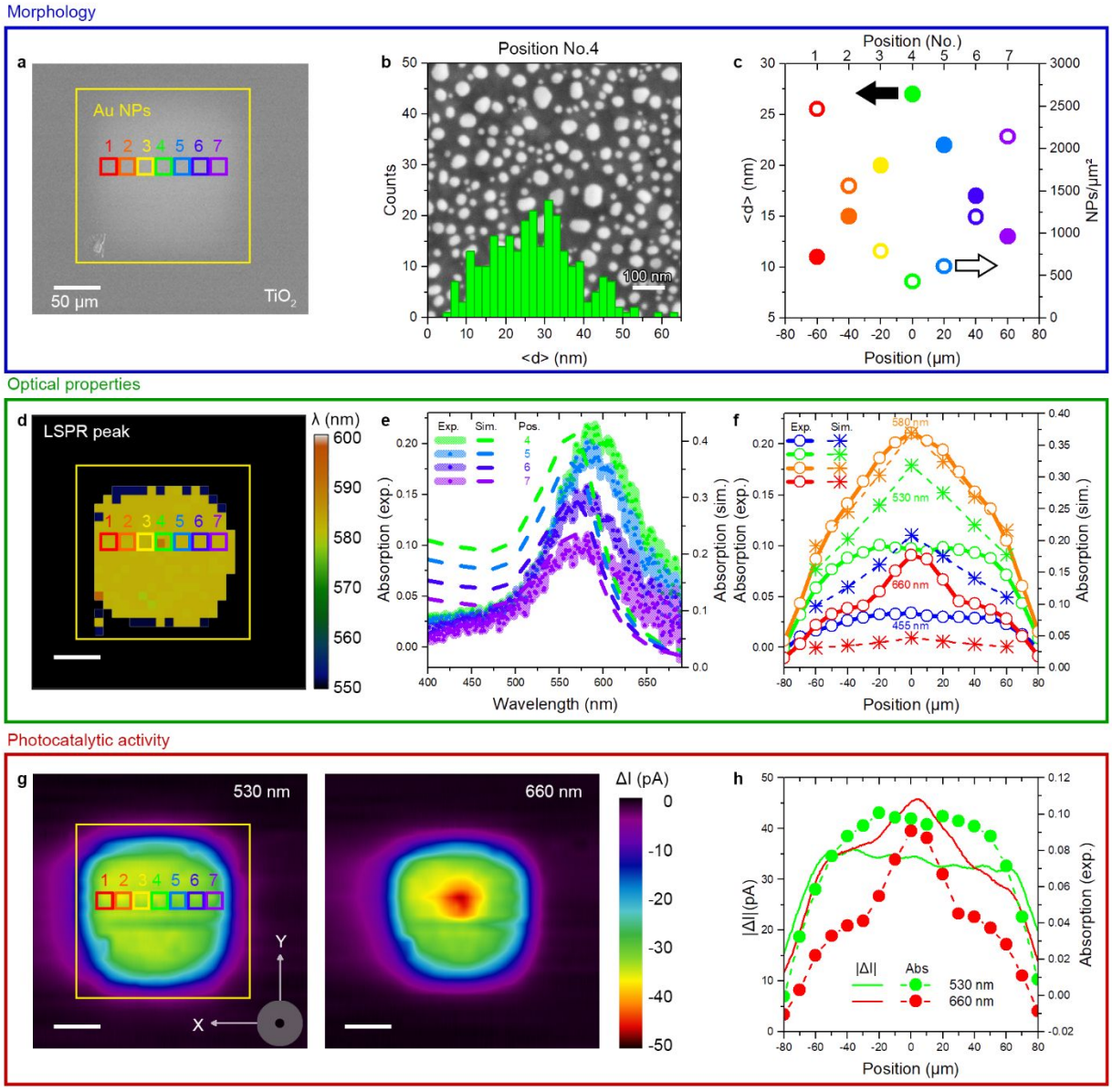

Figure 2. Spatial mapping of the morphology, optical properties and photochemical activity of the planar Au/TiO_2 photocatalysts. **a**, SEM image of the Au NPs Square A on TiO_2/ITO substrate. **b**, SEM image and Au NPs size distribution for position 4 in (**a**). **c**, Mean diameter, <d>, (left axis, filled circles) and population density, NPs/μm², (right axis, empty circles) of the Au NPs retrieved from the corresponding SEM images taken at different positions in (**a**). **d**, LSPR peak map showing the different positions as in (**a**). **e**, Experimental (left axis, dots underlined by solid lines) and calculated (right axis, dashed lines) absorption spectra at different

positions. **f**, Experimental (left axis, empty circles with solid lines) and calculated (right axis, stars with dashed lines) absorption from the line scan across the center of the square at different wavelengths. **g**, Photoactivity maps of (**a**) with Probe 1 (depicted on scale) under monochromatic excitation at 530 and 660 nm with 4.7 μW power. SPECM measurements were done by SG-TC mode with Probe 1, E_T = 0 V vs Ag/AgCl, d = 20 μm and v_{scan} = 20 μm/s in an aerated solution of 1 mM $Fc(MeOH)_2$ and 0.1 M KCl. **h**, Photoactivity (left axis, solid lines) and absorption (right axis, dashed lines with filled circles) at the same line scan position for 530 (green labels) and 660 (red labels) nm. All the maps have the same scale bar.

The plasmon-driven photoactivity maps recorded over Square A (Figure 2g) showed an activity gradient depending on the position within the square and, as expected, a wavelength dependency[21]. The activity over the TiO_2 layer is near-zero, while it increased from the border to the center of the Au NP array, especially for the map recorded at 660 nm. Interestingly, both the photoactivity line scans at 530 and 660 nm closely resembled the corresponding absorption intensity (Figure 2h). When the TiO_2 layer was replaced by Al_2O_3 to prevent the injection of hot electrons through the Schottky barrier ($\phi_{B-TiO_2} \approx 1.1$ eV vs $\phi_{B-Al_2O_3} > 4$ eV)[38], negligible photoactivity was observed (Figure S13a,b). Similarly, no photoactivity was observed when we tested Au NP array on ITO (Figure S13c). This revealed the key role of the Schottky barrier in regulating the separation of plasmonic hot carriers and, in turn, in increasing their lifetime and availability for chemical reactions.

Due to the modest light intensity we adopted (< 7.5 W/cm²), thermal effects were negligible with a ΔT below 0.5 K, which induced a relative current drift lower than 2% due to mass transport[39]. Next, from the measured ΔI, we retrieved the substrate current (I_{Sub}) through a diffusion model for the SG-TC mode (Figure S14) obtaining the calculated values of the collection efficiency

(see Methods)[40] for the molecular species diffusing from the plasmonic substrate to the UME (Table S3). Applying this procedure, the measured ΔI can be associated with the number of hot holes involved into the oxidation of $Fc(MeOH)_2$, thus enabling to compute external quantum efficiency (*EQE*) and the internal quantum efficiency (*IQE*).

Several squares showing different Au NPs size distribution and population density (Figure S15) were investigated to gain insights on how they affected the photoactivity and *QE*s (Figure 3a–c and Figure S16–S21 for Squares A to E). The maps for Square A (Figure 3a,S17 and Figure S18a for Square B) highlighted that the highest *EQE* values fall in the center of the Au NP array at 595 nm (*EQE*~0.015%), i.e., the LSPR wavelength. Both the *EQE* scan profiles at a fixed wavelength and the *EQE* action spectra matched well to the experimental absorption (Figure 3b,c and S18b,c) except for 455 nm. A highest *EQE* of 0.06% was recorded for Square E (Figure S21, morphology in Figure S15c), a value in agreement with previous reports [12,21,38]. The activity dependence on the Au NPs size and distribution was consistent for many investigated squares (Figure S22).

The evaluation of *IQE* line scan plots (Figure 3d and S18d for Squares A and B, respectively) provided further insights into the structure-activity relationship of our planar Au/TiO_2 photocatalysts. As expected, the *IQE* line scans at all investigated wavelengths (455, 530, 595, and 660 nm) showed an inversion of trend in comparison to the *EQE* curves, corresponding to the inverse of the Au NPs size (Figure 3d), with the maximum observed at the edge of the Au NP squares. This result confirmed that smaller particles have higher probability to generate hot carriers through surface scattering (Landau damping) due to their higher surface to volume ratio[6,41]. The highest *IQE* was ~1.6% and was obtained for Square B because of the smaller, denser and homogeneously distributed Au NPs (Table S1). Interestingly, the *IQE* values at 660

nm were always higher than those obtained at 595 nm (closely matching the LSPR) and at 530 nm as the detrimental effect of interband transitions is mitigated at longer wavelengths[42]. In contrast, they were lower than the *IQE* values at 455 nm for Square A, while higher in case of Square B.

To better explain these observations, we used a consolidated quantum mechanical formalism developed by Govorov and co-workers (see Methods)[43,44], to compute the generation rates of both the plasmonic over−barrier hot electrons (that can be approximated as the generation rate of hot holes surviving recombination at the surface) and the d−holes from interband transitions for various Au NPs size (Figure 3e,S9,S23-S29 and Table S2, see Supplementary Video 1) corresponding to the experimental data taken at different position in Square A (Figure 3f,S2-S5,S12,S15a and Table S1). The theoretical curves highlighted that the experimental *EQE*s are a convolution of the photoactivity due to both d-holes and plasmonic hot holes (Figure 3g). They are in good agreement with the experimental *EQE* plots whether we considered the line scan plots or the action spectra (Figure 3g,h,S30 and S31). Furthermore, Figure 3h shows that the generation rates for d−holes can reach up to one order of magnitude higher values than those of plasmonic hot electrons. Considering the ratio between the generation rates of over barrier hot electrons and d-holes at every position, we observed that for λ<650 nm d-holes dominated over the former hot carriers, while for λ>650 nm the plasmonic hot carriers became predominant over those related to interband transitions (Figure S31c).

However, interband transitions occur in the whole NP volume while hot carriers are predominantly generated at the surface, thus possibly prevailing under excitation at shorter wavelengths. This might explain our *IQE* trends showing higher values at 455 nm (Square A),

except in the case where the Au NPs were very small and close to 10 nm in average size (Square B), where the plasmonic *IQE* at 660 nm assumed the highest values.

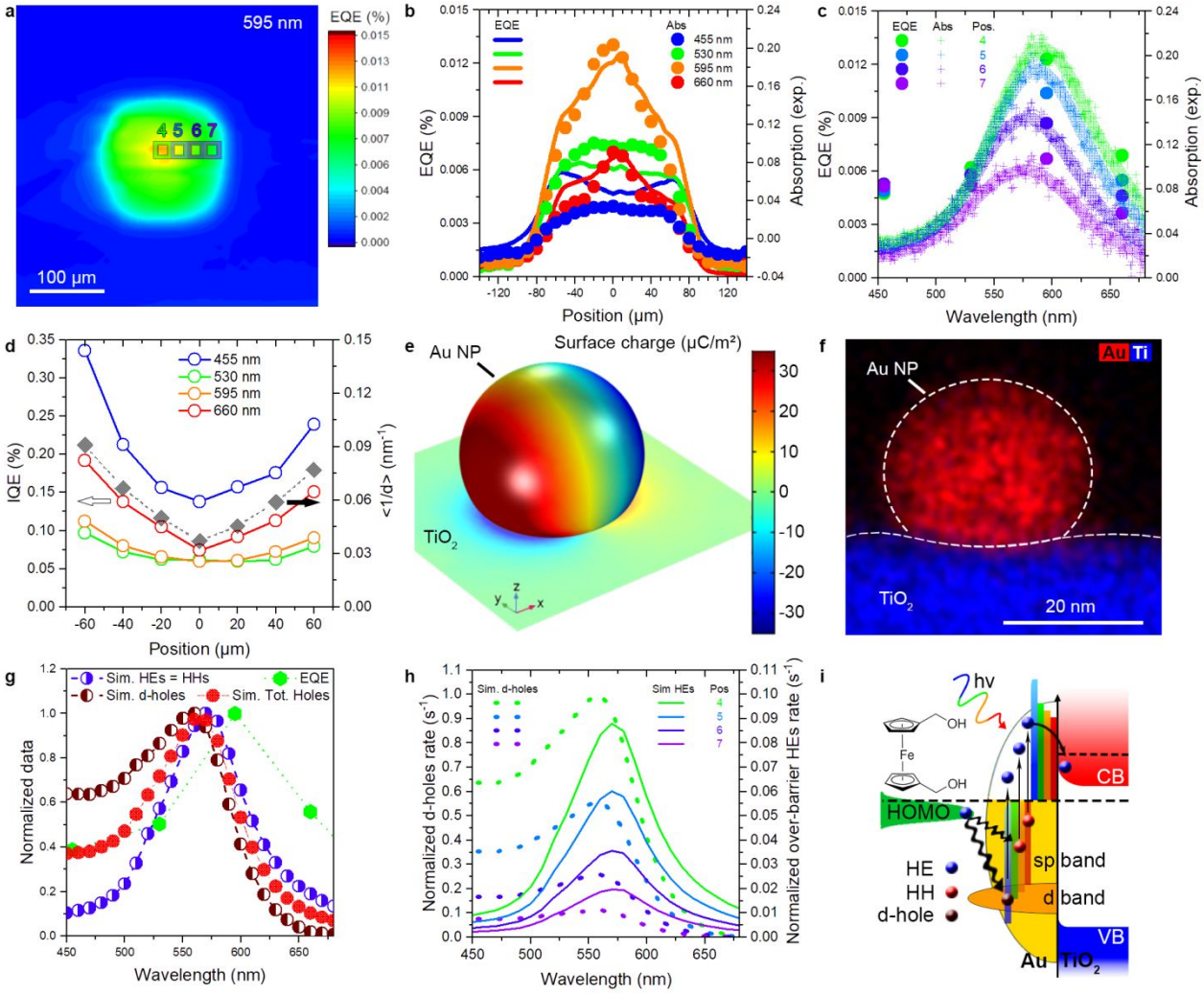

Figure 3. Photochemical quantum efficiency and theoretical modeling. **a**, External quantum yield (*EQE*) map at 595 nm for planar Au/TiO_2 Square A. **b**, *EQE* (left axis, solid lines) along with absorption (right axis, filled circles) for the same line scan position (center of Y axis) at different wavelengths for Square A. **c**, *EQE* (left axis, filled circles) and absorption (right axis, crosses underlined by solid lines) spectra at the different positions represented in (**a**). **d**, Internal quantum yield (*IQE*) (left axis, empty circles with solid lines) for the same line scan position

(center of Y axis) at different wavelengths compared with <1/d> (right axis, solid diamonds with dotted lines) for Square A. **e**, Simulated surface charge map excited at the plasmon peak (564 nm) from a single Au NP corresponding to the position 4 in Square A. **f**, HR-TEM elemental map of a single NP corresponding to the position 4 in Square A. **g**, Normalized comparison of both experimental *EQE* (filled hexagon and solid line) with the calculated over−barrier hot electrons (right half-filled circles with dashed line), d-holes (left half-filled circles with dashed line) and the total of holes (combination of HHs and d-holes, filled circle with solid line) generation rates at position 4 of Square A. **h**, Normalized calculated d-holes (left axis, dotted lines) and over−barrier hot electrons (right axis, solid lines) generation rates spectra corresponding to the different positions in Square A. **i**, Schematic of the wavelength−dependent photochemical mechanism in planar Au/TiO_2.

To extend our methodology to energetically demanding reactions, we investigated both the plasmonic–driven chlorine and water oxidation, which are also known for their sluggish kinetics (Table S4). The photoactivity maps previously obtained in $Fc(MeOH)_2$ and KCl reflected the detection of the $Fc(MeOH)_2^+$ photoproduced at the Au/TiO_2 surface. In contrast, by using electrolytes composed by (a) KCl or (b) $KClO_4$, we obtained photoactivity maps due to the detection of (a) Cl_2 and H_2O_2/O_2 or (b) only H_2O_2/O_2, respectively, produced by plasmonic oxidation reactions (Figure S32). These measurements revealed the possibility to drive challenging chemical transformations using plasmonic hot holes, despite with lower efficiencies if compared to the oxidation of $Fc(MeOH)_2$. Moreover, such experiments provided insights into the wavelength–dependent mechanism that changed depending on the investigated reaction, with the peak efficiency observed for hot holes deriving mainly from interband transitions excited at 455 nm instead that at the LSPR.

Photoactivity mapping of a single plasmonic Au/TiO_2 nanodiode

In the next step, we coupled our methodology with the use of a nanoprobe to unlock the hot carrier reactivity mapping over a single plasmonic hybrid nanostructure with nanoscale resolution. First, Au NPs were deposited by sputtering on self-standing separated TiO_2 nanotube arrays. Afterwards, the nanotubes were scratched from their support (Ti foil) and then dropcasted onto the TiO_2/ITO surface (Figure 4a). The SEM image of a single nanotube and the corresponding EDS spectra taken at different positions within the nanostructure highlighted the formation of an Au NPs gradient (Figure S33). HR-TEM images and EDS elemental mapping (Figure 4b,c and S34-S38) further confirmed the formation of an Au NPs population gradient from top to bottom of the TiO_2 nanotubes as a consequence of the tube length (~ 3–4 μm). This feature was observed for all the investigated Au/TiO_2 nanotubes (Figure 4b,c and S33-S39). Through this gradient and the presence of a rectifying junction at the Au/TiO_2interface, we expected to observe a diode–like behavior due to the hot charge carrier spatial separation between the area containing Au NPs and the one with only TiO_2. Using a microprobe, we identified the position (Figure S40a) and correlated it with the photoactivity map (Figure S40b) of various single nanotubes. Remarkably, by switching to the nanoprobe over specific positions, we had access to the localized photoactivity map of a single nanostructure (Figure S33a and Figure S39 for SEM and Figure S33b and S41 for SPECM images, respectively), which revealed different photocatalytic activity at varying positions over the Au NPs/TiO_2 nanotube. The concentration modification of $Fc(MeOH)_2^+$ in solution directly influenced the measured probe current. We observed areas with increased or decreased probe current (I_{Tip}) in comparison with the dark current (Figure S42). Increased I_{Tip} corresponded to a local decrease of $Fc(MeOH)_2^+$ due to its reduction by hot electrons from the nanostructure, whereas decreased I_{Tip} corresponded to a

local increase of $Fc(MeOH)_2^+$ due to $Fc(MeOH)_2$ oxidation by hot holes from the nanostructure. The nanostructure position on the TiO_2/ITO substrate did not impact the investigation: the photoactivity due to hot holes was detected where Au NPs were the densest, whereas the one related to hot electrons was detected where the TiO_2 nanotube was almost barren of Au NPs (Figure S33-S41).

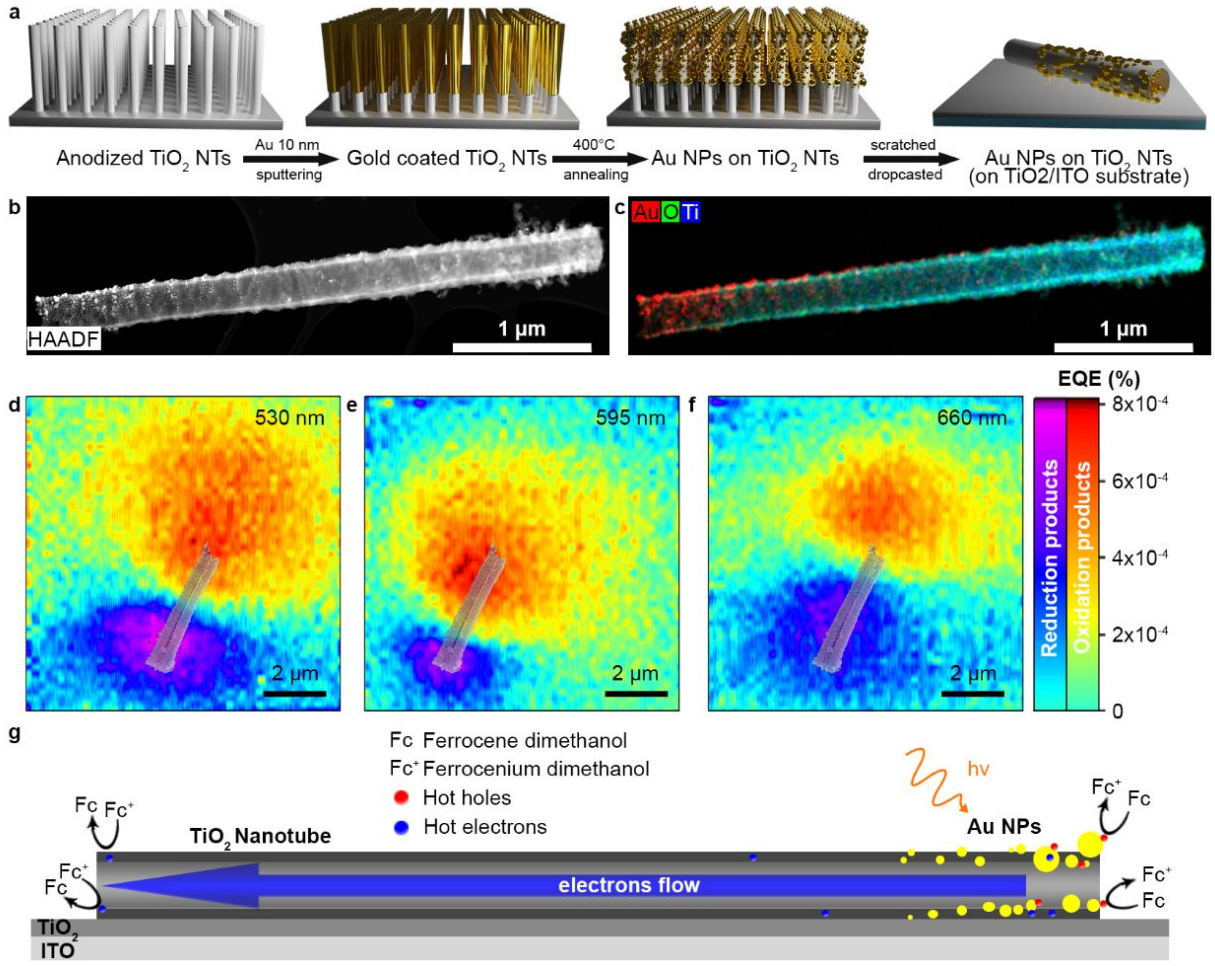

Figure 4. Photochemical nanoscopy of isolated plasmonic photocatalysts: Au−decorated TiO_2 nanotubes. a, Fabrication scheme of Au-decorated TiO_2 nanotubes deposited on TiO_2/ITO substrate. **b**, HAADF image and **c**, elemental mapping for the Au (red), Ti (blue) and O (green) elements of a single Au/TiO_2 nanotube . **d-f**, *EQE* maps of a single nanostructure obtained for

light excitation at 530 (**d**), 595 (**e**) and 660 (**f**) nm using 4.7, 5 and 4.7 μW power, respectively. **g**, Schematic of the hot charge carriers transfer in the plasmonic diode model. The SEM image of the structure is overlayed on (**d-f**) at the same scale than *EQE* maps.

Furthermore, the plasmonic nanodiode was investigated at different wavelengths (Figure 4d-f and Figure S41) to highlight the impact of the excitation wavelength on the plasmonic reactivity. The highest activity due to hot holes was observed at 595 nm, while the lowest was at 660 nm. Interestingly, the *EQE* line scan profiles (Figure S43) revealed similar values for the efficiency maxima associated to the hot holes and hot electrons. This suggests that the same number of plasmonic hot holes and electrons survive recombination and participate to photocatalysis.
We propose the following mechanism underlying the observed plasmonic nanodiode behavior. Upon plasmon decay, hot holes at the surface of the Au NPs oxidize $Fc(MeOH)_2$, while hot electrons injected through the Au/TiO_2 Schottky barrier travel by ballistic diffusion (tens of μm)[45–47] through the length of the TiO_2 nanotube. Eventually, the latter reach the bottom of the tube and undergo chemical reaction at the surface, reducing $Fc^+(MeOH)_2$ (Figure 4g).

Conclusions

We realized the *in situ* nanoscale mapping of photocatalytic chemical products evolved from plasmonic photocatalysts with subwavelength resolution. The presented methodology is based on a unique ensemble of scanning microscopies enabling to build structure–activity relationships among morphological, optical and photochemical properties. By investigating planar Au/TiO_2 photocatalysts and using an approach combining experiments and theory, we demonstrated that smaller and denser plasmonic nanoparticle arrays present lower absorption, but higher internal quantum efficiency for hot hole–driven photocatalysis. We found that at lower wavelength the d–holes played a significant role in photocatalysis, while plasmonic hot holes were predominant at

longer wavelengths. Notably, the highest photocatalytic quantum yield for the oxidation of ferrocene dimethanol corresponded to the plasmon peak, whereas energetically and kinetically demanding reactions like water and chlorine oxidation were driven by d–holes with higher efficiency. By imaging the photoactivity of a single nanostructure, we showed the possibility to visualize oxidation and reduction product areas over the same Au/TiO_2 nanotube. Our approach can be extended to a vast variety of chemical reactions by adapting the experimental conditions. We anticipate that the present methodology can be generalized to a wide range of low–dimensional materials for energy and sensing, opening to a nanoscale rationale for the design of efficient photoactive nanomaterials.

Methods

Planar Au-TiO_2 nanostructures fabrication. The planar Au-TiO_2 plasmonic photocatalysts were prepared on 25x25 mm² ITO coated glass (Ossila, UK). The ITO coated glass substrates were cleaned by ultrasonication in acetone, ethanol then deionized water for 5 minutes each. A TiO_2 layer of 30 nm was deposited by by plasma-assisted atomic layer deposition (ALD, Ultratech/CambridgeNanoTech Fiji 200) using tetrakis(dimethylamido)titanium as precursor (99% purity, Strem, USA) at 250 °C. An ALD cycle consisted of 0.1 s of precursor exposure, 5 s purge, 20 s O_2 plasma exposure (300 W), and 5 s purge of reaction products. The so-obtained TiO_2 thin layers were annealed at 450°C (2°C/min) for 2 h to insure TiO_2 anatase phase formation. The Au NP arrays were formed upon annealing at 400°C (2°C/min) for 1 h of a 10 nm thick Au film sputtered through a patterned mask (Micronlaser Technology, USA) divided into 16x16 squares (around 100x100 µm² spaced by 400 µm).

Au decorated-TiO_2 nanotubes fabrication. Spaced TiO_2 nanotubes are prepared on titanium foil by anodization with a two-electrode electrochemical cell in which Ti foil (0.25 mm thick) is used as a working electrode and Pt foil serves as counter electrode. Firstly, the commercial Ti foil is washed by sonication in acetone, ethanol, and distilled water for about 15 min and then dried under a nitrogen stream. Secondly, the foil is anodized in diethylene glycol electrolyte containing 0.5 wt.% NH_4HF_2 and 3.6 wt.% H_2O at an applied voltage of 60 V for 3h at 40°C. After anodization, the sample is washed with ethanol and dried by a nitrogen stream. Later on, the spaced TiO_2 nanotubes are annealed under air at 450°C (2°C/min) for 2 h to prepare crystalline TiO_2 nanotubes. The spaced TiO_2 nanotubes are coated with 10 nm of Au then annealed at 400°C (2°C/min) for 1 hour under air. The nanotubes are scratched from the foil and dispersed in distilled water then drop-casted on TiO_2/ITO substrate. The optical properties of the Au/TiO_2 nanotubes were investigated at every step of the fabrication by ultraviolet-visible-near infrared spectroscopy retrieving the absorptance from reflectance spectra measured with an integrating sphere (Figure S44).

Morphological characterization. A field emission scanning electron microscope (FE-SEM, Hitachi SU 6600, Japan) was used to investigate the nanomaterials morphology. The Au size distribution was

obtained by ImageJ applying a filter depending of the observed contrast. The calculated diameter were retrieved from the area of the NPs measured by ImageJ by approximating all NPs shape to a circumference. The composition and morphology of the investigated Au/TiO_2 systems were verified through high-resolution transmission electron microscopy (HR-TEM) (Titan G2, FEI), by TEM measurements and EDS elemental mapping. A BM Ultra-Scan CCD camera (Gatan) was used to capture the elemental maps. The preparation of lamellae from planar Au/TiO_2 was carried out with a focused ion beam SEM (Scios 2 DualBeam, ThermoFisher SCIENTIFIC). The area of interest was coated by platinum (electron beam deposition) with a gas injection system. The sample was tilted by 52° and the milling process was performed to obtain lamellae from the bulk samples. The lamellae were undercut and removed from the bulk material by micromanipulator and attached to the TEM grid. After the welding of lamellae to the grid, the lamellae were thinned through a step-by-step ion milling process with decreasing currents until it was transparent to the accelerated electron beam. The Au/TiO_2 nanotubes were prepared by scratching the anodized film and dispersed in distilled water then drop-casted on the TEM grid.

Scanning spectrophotometer microscopy (SSM). The optical properties were measured with a spectrophotometer coupled with the scanning photoelectrochemical microscope position system to locally investigate the substrate (HEKA Gmbh, Lambrecht, Germany). SSM consists of a white light focused below the sample and aligned with the spectrophotometer above it to collect the transmitted light. The illumination beam radius was ~ 10 µm and the lamp used was a Lambda DG 4 Xenon Arc bulb (wavelength from 330 to 670 nm, Sutter instruments, USA). The absorption maps were generated thanks to the localized transmission spectra at different XY positions of the sample (every 10 µm). From those spectra, the absorption values from the wavelength of interest was extracted and combined together depending of their XY position to form the absorption maps. The LSPR peak from plasmonic nanostructures were extracted similarly by taking the maximum absorption measured for each spectra. Due to the white lamp limitation, we were able to investigate wavelengths from 400 to 670 nm.

Scanning photoelectrochemical microscopy (SPECM). The SPECM employed the same optical path below the sample than SSM to focus the LED light beam (~ 5 µm radius) with a 40x objective lens

(Olympus, Japan) to locally irradiate the sample and drive the photochemical reactions. SPECM experiments were conducted using an ELP 3 SPECM-FL (HEKA Elektronik GmbH, Lambrecht, Germany), a PG 618 USB bipotentiostat (HEKA Elektronik GmbH, Lambrecht, Germany) and fiber-coupled LED lamps with different wavelengths: 455 ± 7, 530 ± 15, 595 ± 40, 660 ± 9, 740 ± 11 and 850 ± 15 nm (Thorlabs, USA). The experiments were performed in aerated solution of 0.1 M KCl and 1 mM $Fc(MeOH)_2$ (ferrocene dimethanol, $FeC_{12}H_{14}O_2$), unless told otherwise. Chemicals were bought from Sigma Aldrich with the highest purity and used without further purification. Milli-Q water was used for the preparation of all aqueous solutions. SPECM consists of a four-electrode setup with two working electrodes (WE): the substrate (WE1, not connected in this study) and the ultramicroelectrode (WE2), a Ag/AgCl wire used as reference electrode and a Pt wire as counter electrode. Three different ultramicroelectrodes (from HEKA Elektronik GmbH, Lambrecht, Germany) were used in this work: Probe 1 (r_T = 5 µm and RG = 5), Probe 2 (r_T = 5 µm and RG = 25) and Probe 3 (r_T = 100 nm and RG = 25). The probe moves in the vicinity of the studied sample to detect the local species concentration in solution. The light beam and the probe were aligned before measurements. The samples were scanned on the XY stage while the probe was placed at a constant height (d) using the Z stage. The redox mediator is oxidized (reduced) from the hot holes (electrons) as follow:

$$Fc(MeOH)_2 + h^+ \rightarrow Fc^+(MeOH)_2 \qquad (1)$$

This locally modifies the concentration of both species (reduced and oxidized) in the vicinity of the beam position. The probe detects this reaction by reducing (oxidizing) back (substrate generation – tip collection, SG-TC mode) the species produced by the substrate:

$$Fc^+(MeOH)_2 + e^- \rightarrow Fc(MeOH)_2 \qquad (2)$$

The probe is biased at a potential (E_{Tip}) corresponding to the diffusion limited regime (0 and 0.4 V vs Ag/AgCl for SG-TC and RC modes, respectively), i.e. the plateau in Figure 1d. Thus, the probe current (I_T) corresponds to a steady-state regime and is given by equation 3 in solution ($I_{T,\infty}$) and equation 4 near

the substrate ($I_{T,ins}$) due to the hindering effect on the diffusion of both the substrate and the probe (corresponding to negative feedback)[29,48]:

$$I_{T,\infty} = 4nFCDr_T \qquad (3)$$

$$I_{T,ins} = 4nFCDr_T\beta(RG)Ni_T(L,RG) \qquad (4)$$

where n is the number of electrons involved; F, the faraday constant (96485.33 C/mol); C, the concentration in Red/Ox species; D, the diffusion coefficient of the Red/Ox species (7.8×10^{-6} cm²/s)[49]; r_T, the probe active part radius; RG, the ratio between the probe insulating part radius and r_T; $\beta(RG)$, the RG impact on the diffusion to the probe active area and $Ni_T(L)$, the hindering effect of the near surface on the probe current with L corresponding to the ratio between the distance probe-substrate (d) and r_T. In the case of redox competition (RC) mode, the probe detects the concentration evolution of $Fc(MeOH)_2$ following equation 1. The photochemical map acquisition were done with an XY scan method consisting of 1001 acquisitions in X and 41 lines in Y. The probe was scanning at determined scan speed (v_{scan}). The number of acquisitions and lines in XY depends of the map size and the intended resolution. In the case of 400x400 µm² maps, an acquisition was made every 0.4 µm in X and 41 lines in Y were measured to have a step size of 10 µm (diameter of the active part of Probe 1) between each line. In the case of the Au-decorated TiO_2 nanotube investigations, the maps consists of 501 acquisitions in X and 51 lines in Y (meaning 1 acquisition every 20 nm in X and 200 nm in Y). The dark current map is available in Figure S45. The Z axis position was constant through the scan and was determined by approach curves nearby the zone of interest thanks to the negative feedback observed due to the TiO_2 insulating properties. Because of the background noise for the nanoscale maps, the data were smoothened using the averaging function for 10 points from origin.

Diffusion model. The diffusion model was simulated with COMSOL Multiphysics using the "Transport of Diluted Species" physics in a 2D asymmetric mode considers the substrate as an electrochemical object corresponding to the light beam size (Figure S14a). This simulation model gives information such as the ratio between the probe current and the substrate current (called collection efficiency, CE, equation 5), the

probe geometry influence and the impact of the probe-substrate distance on the CE (Figure S14b). In the case of Probe 1, the CE is considered 100% when the probe nearly touches the substrate due to the identical probe and light beam size[40] consequently the probe current measured near the substrate is considered as the substrate current to compare experimental data (approach curves) and simulation data (see Figure S14c). The diffusion profiles (Figure S14d-f, d for d = 40 µm, e for d = 2 µm with the Probe 1 and f for d = 2 µm with the Probe 3) highlight the impact on the CE from the probe geometry. CE refers to the ability of the probe to collect species produced by the substrate and is defined as the probe current divided by the substrate current:

$$CE(\%) = \frac{I_T}{I_{Sub}} \times 100 \qquad (5)$$

As presented in Table S3, I_{Sub} increases when the Probe 1 is closer to the substrate with an increase of 40% for d = 5 µm and I_T is higher than the current corresponding to the initial concentration present in solution due to the recycling effect from the active part of the probe. To avoid this effect, every measurement with the Probe 1 were done with d ≥ 10 µm. From the obtained CE, I_{Sub} was calculated thanks to the measured ΔI. The external quantum efficiency (EQE) and internal quantum efficiency (IQE) were calculated from the following equations:

$$EQE\ (\%) = \frac{I_{Sub}/e}{P/hv} \times 100 \qquad (6)$$

$$IQE\ (\%) = \frac{EQE\ (\%)}{Absorption} \qquad (7)$$

where e is the charge of one electron, P is the light power and hv is the photon energy.

Electromagnetic and hot-carrier simulations. The theoretical modeling was computed with COSMOL Multiphysics. The system consists of a periodic array of truncated nanospheres on a substrate (Figure S9). For each sample, a fixed nanoparticle (NP) size and array periodicity were chosen based on the averaged NPs from Position 1 to 7 in Square A, and are presented on Table S2, along with other relevant geometric parameters. The incident light intensity was fixed at 10^5 W/m^2 and its direction is perpendicular to the NP-substrate interface, coming up from the bottom, as shown in Figure 1a. The surrounding medium is an

electrolyte with a dielectric constant equal to 1.8171, while the substrate dielectric constant is 3.69. This parameter was chosen by considering the substrate an effective medium, taking TiO_2 and ITO into account. To begin the computation, the considered electric field inside and outside of the nanostructure has the following form:

$$\boldsymbol{E}(\boldsymbol{r}) = \boldsymbol{E}_{\omega} e^{-i\omega t} + \boldsymbol{E}_{\omega}^{*} e^{+i\omega t} \qquad (8)$$

The absorption power is then given by

$$Q_{abs} = \left\langle \int_{NP} \boldsymbol{j} \cdot \boldsymbol{E}\, dV \right\rangle_{time} \qquad (9)$$

where $\boldsymbol{j}$ is the current inside the NPs. Then, given the light intensity I_0, the absorption cross section is expressed as

$$\sigma_{abs} = \frac{P_{abs}}{I_0} \qquad (10)$$

Additionally, the optical extinction is a combination of the absorbed and scattered light. Therefore, the extinction cross section is a sum, as shown below:

$$\sigma_{ext}(\omega) = \sigma_{abs}(\omega) + \sigma_{scat}(\omega) \qquad (11)$$

As part of the light absorption process, there is a generation of hot electrons, which occurs near the NP surface[43,44]. The rate of this generation is then expressed as

$$\text{rate}_{\text{HE}} = \frac{2}{\pi^2}\frac{e^2 E_F^2}{\hbar}\frac{1}{(\hbar\omega)^3}\int_{S_{NC}} |E_{\omega,normal}(\theta,\phi)|^2 ds, \qquad (12)$$

where e is the electron charge, E_F is the Fermi energy (5.5 eV for Au) and $E_{\omega,normal}$ is the normal electric field. However, in many cases we are more interested in the hot electrons that possess a high enough energy to overcome an energy potential (ΔE_{bar}) and therefore, be transferred to another material. The rate of generation of these types of hot electrons is given by,

$$rate_{HE,over-barrier} = \frac{2}{\pi^2}\frac{e^2 E_F^2 (\hbar\omega - \Delta E_{bar})}{\hbar}\frac{}{(\hbar\omega)^4}\int_{S_{NC}} |E_{\omega,normal}(\theta,\phi)|^2 ds, \qquad (13)$$

where the energy barrier was given a value of 1 eV in this study. For the interband d-hole mechanism, the expressions for the rates are given by this equation[43,44]:

$$Rate_{\text{d-holes, bulk}} = \varepsilon_0 \frac{1}{\mathrm{h}\omega} \mathrm{Im}\,\Delta\varepsilon_{\text{interband}}(\omega) \frac{\omega}{2} \int_{\text{NP}} dV\ \mathbf{E}_\omega \cdot \mathbf{E}_\omega^* \qquad (14)$$

Here $\Delta\varepsilon_{\text{interband}}$ is the interband contribution to the bulk dielectric constant.

Moreover, the dielectric function used on the computation of the generation rates of hot electrons incorporates a quantum surface-scattering effect that must be considered in the light dissipation. With this approach, the local dielectric function is given by

$$\varepsilon_{metal}(\omega) = \varepsilon_{metal,bulk}(\omega) + \frac{\omega_p^2}{\omega(\omega + i\gamma_D)} - \frac{\omega_p^2}{\omega(\omega + i(\gamma_D + \gamma_s))} \qquad (15)$$

where $\varepsilon_{metal,bulk}$ is the empirical dielectric constant, ω_p is the plasmon frequency, γ_D is the Drude broadening, and γ_s is the quantum plasmonic broadening. The last parameter is the one responsible for the incorporation of the scattering of electrons at the NP surface, which is size-dependent.

Finally, the surface charge distribution maps were also computed with COMSOL Multiphysics with the following expression

$$\sigma = E\varepsilon_0 \qquad (16)$$

Data Availability

The data that support the findings of this study are available from the corresponding authors upon request.

AUTHOR INFORMATION

Corresponding Authors

Olivier Henrotte − *Czech Advanced Technology and Research Institute, Regional Centre of Advanced Technologies and Materials Department, Palacký University Olomouc, Šlechtitelů 27, Olomouc 78371, Czech Republic*; Email: olivier.henrotte@upol.cz

Alberto Naldoni − *Czech Advanced Technology and Research Institute, Regional Centre of Advanced Technologies and Materials Department, Palacký University Olomouc, Šlechtitelů 27, Olomouc 78371, Czech Republic; Department of Chemistry and NIS Centre, University of Turin, Turin 10125, Italy*; Email: alberto.naldoni@unito.it

Authors

Eva Yazmin Santiago − *Department of Physics and Astronomy, Nanoscale and Quantum Phenomena Institute, Ohio University Athens, Ohio 45701, United States*

Artur Movsesyan − *Department of Physics and Astronomy, Nanoscale and Quantum Phenomena Institute, Ohio University Athens, Ohio 45701, United States; Institute of Fundamental and Frontier Sciences, University of Electronic Science and Technology of China, Chengdu 610054, China*

Luca Mascaretti − *Czech Advanced Technology and Research Institute, Regional Centre of Advanced Technologies and Materials Department, Palacký University Olomouc, Šlechtitelů 27, Olomouc 78371, Czech Republic*

Morteza Afshar − *Czech Advanced Technology and Research Institute, Regional Centre of Advanced Technologies and Materials Department, Palacký University Olomouc, Šlechtitelů 27, Olomouc 78371, Czech Republic*

Alessandro Minguzzi − *Laboratory of Applied Electrochemistry, Dipartimento di Chimica, Università degli Studi di Milano, via Golgi 19, Milano 20133, Italy; Consorzio Interuniversitario Nazionale per la Scienza e Tecnologia dei Materiali, via Giusti 9, Firenze – Italy*

Alberto Vertova − *Laboratory of Applied Electrochemistry, Dipartimento di Chimica, Università degli Studi di Milano, via Golgi 19, Milano 20133, Italy; Consorzio Interuniversitario Nazionale per la Scienza e Tecnologia dei Materiali, via Giusti 9, Firenze – Italy*

Zhiming Wang − *Institute of Fundamental and Frontier Sciences, University of Electronic Science and Technology of China, Chengdu 610054, China*

Radek Zbořil − *Czech Advanced Technology and Research Institute, Regional Centre of Advanced Technologies and Materials Department, Palacký University Olomouc, Šlechtitelů 27, Olomouc 78371, Czech Republic; CEET, Nanotechnology Centre, VŠB-Technical University of Ostrava, 17. Listopadu 2172/15, Ostrava-Poruba 708 00, Czech Republic*

Štěpán Kment − *Czech Advanced Technology and Research Institute, Regional Centre of Advanced Technologies and Materials Department, Palacký University Olomouc, Šlechtitelů 27, Olomouc 78371, Czech Republic; CEET, Nanotechnology Centre, VŠB-Technical University of Ostrava, 17. Listopadu 2172/15, Ostrava-Poruba 708 00, Czech Republic*

Alexander O. Govorov − *Department of Physics and Astronomy, Nanoscale and Quantum Phenomena Institute, Ohio University Athens, Ohio 45701, United States*

Author contributions

O.H and A.N. conceived and designed the experiments. A.N. coordinated and supervised the project. O.H. performed the samples preparation, SPECM measurements, and analyzed the data. L.M. performed the atomic layer depositions. M.A. performed the TiO_2 nanotubes fabrication. L.M and M.A. performed the optical spectroscopy measurements. A.M. and A.V. performed the

diffusion model simulations. E.Y.S., A.M. and A.O.G. performed electromagnetic simulations and hot carrier generation theory. O.H. prepared the figures and wrote the first draft. All authors discussed and edited the manuscript.

Acknowledgements

The authors acknowledge the support of the Czech Science Foundation (GACR) through the award n. 22-26416S and the Ministry of Education, Youth and Sports of the Czech Republic and the Operational Programme Research, Development and Education - European Regional Development Fund, project no. CZ.02.1.01/0.0/0.0/15_003/0000416. The authors thank Eirini Ioannou and Jiří Hošek for the SEM measurements, Jiří Hošek and Tomanec Ondřej for the HR-TEM measurements and Mareike Haensch for the SSM measurements. The authors acknowledge CzechNanoLab Research Infrastructure supported by MEYS CR (LM2018110). A.M. And A.V. acknowledge the financial support of MUR – PRIN 2017, Prot. 2017YH9MRK: ‘‘Novel Multilayered and Micro-Machined Electrode Nano-Architectures for Electrocatalytic Applications (Fuel Cells and Electrolyzers)’’ and of the Università degli Studi di Milano, Piano di Sostegno alla Ricerca, linea 2A. A.M. and Z.W. were supported by the National Key Research and Development Program of China (2019YFB2203400) and the “111 Project” (B20030).

Competing interests

The authors declare no competing interests.

References

(1) Cortés, E. Efficiency and Bond Selectivity in Plasmon-Induced Photochemistry. *Adv. Opt. Mater.* **2017**, *5*, 1700191. https://doi.org/10.1002/adom.201700191.

(2) Linic, S.; Christopher, P.; Ingram, D. B. Plasmonic-Metal Nanostructures for Efficient Conversion of Solar to Chemical Energy. *Nat. Mater.* **2011**, *10* (12), 911–921. https://doi.org/10.1038/nmat3151.

(3) Jain, P. K. Taking the Heat off of Plasmonic Chemistry. *J. Phys. Chem. C* **2019**, *123* (40), 24347–24351. https://doi.org/10.1021/acs.jpcc.9b08143.

(4) Zhang, Z.; Zhang, C.; Zheng, H.; Xu, H. Plasmon-Driven Catalysis on Molecules and Nanomaterials. *Acc. Chem. Res.* **2019**, *52* (9), 2506–2515. https://doi.org/10.1021/acs.accounts.9b00224.

(5) Zhang, C.; Jia, F.; Li, Z.; Huang, X.; Lu, G. Plasmon-Generated Hot Holes for Chemical Reactions. *Nano Res.* **2020**, *13* (12), 3183–3197. https://doi.org/10.1007/s12274-020-3031-2.

(6) Govorov, A. O.; Zhang, H.; Demir, H. V.; Gun'ko, Y. K. Photogeneration of Hot Plasmonic Electrons with Metal Nanocrystals : Quantum Description and Potential Applications. *Nano Today* **2014**, *9* (1), 85–101. https://doi.org/10.1016/j.nantod.2014.02.006.

(7) Burda, C.; Chen, X.; Narayanan, R.; El-Sayed, M. A. *Chemistry and Properties of Nanocrystals of Different Shapes*; 2005; Vol. 105. https://doi.org/10.1021/cr030063a.

(8) Xia, Y.; Xiong, Y.; Lim, B.; Skrabalak, S. E. Shape-Controlled Synthesis of Metal Nanocrystals: Simple Chemistry Meets Complex Physics? *Angew. Chemie Int. Ed.* **2009**, *48* (1), 60–103. https://doi.org/10.1002/anie.200802248.

(9) Kelly, K. L.; Coronado, E.; Zhao, L. L.; Schatz, G. C. The Optical Properties of Metal Nanoparticles: The Influence of Size, Shape, and Dielectric Environment. *J. Phys. Chem. B* **2003**, *107*, 668–677. https://doi.org/10.1016/j.ocecoaman.2014.06.011.

(10) Xia, Y.; Halas, N. J. Shape-Controlled Synthesis and Surface Plasmonic Properties of Metallic Nanostructures. *MRS Bull.* **2021**, *30* (2005), 338–348. https://doi.org/10.1557/mrs2005.96.

(11) Kreibig, U.; Vollmer, M. *Optical Properties of Metal Clusters*; Springer, Berlin, Heidelberg, 1999. https://doi.org/10.1007/978-0-387-98135-2.

(12) Mubeen, S.; Lee, J.; Singh, N.; Krämer, S.; Stucky, G. D.; Moskovits, M. An Autonomous Photosynthetic Device in Which All Charge Carriers Derive from Surface Plasmons. *Nat. Nanotechnol.* **2013**, *8*, 247–251. https://doi.org/10.1038/nnano.2013.18.

(13) Zhan, C.; Moskovits, M.; Tian, Z.-Q. Perspective Recent Progress and Prospects in Plasmon-Mediated Chemical Reaction. *Matter* **2020**, *3* (1), 42–56. https://doi.org/10.1016/j.matt.2020.03.019.

(14) Angelis, F. De; Das, G.; Candeloro, P.; Patrini, M.; Galli, M.; Bek, A.; Lazzarino, M.; Maksymov, I.; Liberale, C.; Andreani, L. C.; Fabrizio, E. Di. Nanoscale Chemical Mapping Using Three-Dimensional Adiabatic Compression of Surface Plasmon Polaritons. *Nat. Nanotechnol.* **2010**, *5* (1), 67–72. https://doi.org/10.1038/nnano.2009.348.

(15) Giugni, A.; Torre, B.; Toma, A.; Francardi, M.; Malerba, M.; Alabastri, A.; Zaccaria, R. P.; Stockman, M. I.; Fabrizio, E. Di. Hot-Electron Nanoscopy Using Adiabatic Compression of Surface Plasmons. *Nat. Nanotechnol.* **2013**, *8*, 845–852. https://doi.org/10.1038/nnano.2013.207.

(16) Sytwu, K.; Vadai, M.; Hayee, F.; Angell, D. K.; Dai, A.; Dixon, J.; Dionne, J. A. Driving

Energetically Unfavorable Dehydrogenation Dynamics with Plasmonics. *Science (80-.).* **2021**, *371* (6526), 280–283. https://doi.org/10.1126/science.abd2847.

(17) Cortés, E.; Xie, W.; Cambiasso, J.; Jermyn, A. S.; Sundararaman, R.; Narang, P.; Schlücker, S.; Maier, S. A. Plasmonic Hot Electron Transport Drives Nano-Localized Chemistry. *Nat. Commun.* **2017**, *8*, 14880. https://doi.org/10.1038/ncomms14880.

(18) Hamans, R. F.; Parente, M.; Baldi, A. Super-Resolution Mapping of a Chemical Reaction Driven by Plasmonic Near-Fields. *Nano Lett.* **2021**, *21* (5), 2149–2155. https://doi.org/10.1021/acs.nanolett.0c04837.

(19) Oksenberg, E.; Shlesinger, I.; Xomalis, A.; Baldi, A.; Baumberg, J. J.; Koenderink, A. F.; Garnett, E. C. Energy-Resolved Plasmonic Chemistry in Individual Nanoreactors. *Nat. Nanotechnol.* **2021**, *16* (12), 1378–1385. https://doi.org/10.1038/s41565-021-00973-6.

(20) Zhu, H.; Xie, H.; Yang, Y.; Wang, K.; Zhao, F.; Ye, W.; Ni, W. Mapping Hot Electron Response of Individual Gold Nanocrystals on a TiO2 Photoanode. *Nano Lett.* **2020**, *20* (4), 2423–2431. https://doi.org/10.1021/acs.nanolett.9b05125.

(21) Yu, Y.; Wijesekara, K. D.; Xi, X.; Willets, K. A. Quantifying Wavelength-Dependent Plasmonic Hot Carrier Energy Distributions at Metal/Semiconductor Interfaces. *ACS Nano* **2019**, *13* (3), 3629–3637. https://doi.org/10.1021/acsnano.9b00219.

(22) Chikkaraddy, R.; Nijs, B. De; Benz, F.; Barrow, S. J.; Scherman, O. A.; Rosta, E.; Demetriadou, A.; Fox, P.; Hess, O.; Baumberg, J. J. Single-Molecule Strong Coupling at Room Temperature in Plasmonic Nanocavities. *Nature* **2016**, *535* (7610), 127–130. https://doi.org/10.1038/nature17974.

(23) Foerster, B.; Hartelt, M.; Collins, S. S. E.; Aeschlimann, M.; Link, S.; Sönnichsen, C. Interfacial States Cause Equal Decay of Plasmons and Hot Electrons at Gold − Metal

Oxide Interfaces. *Nano Lett.* **2020**, *20*, 3338–3343. https://doi.org/10.1021/acs.nanolett.0c00223.

(24) Tian, Y.; Tatsuma, T. Mechanisms and Applications of Plasmon-Induced Charge Separation at TiO2 Films Loaded with Gold Nanoparticles. *J. Am. Chem. Soc.* **2005**, *127* (20), 7632–7637. https://doi.org/10.1021/ja042192u.

(25) Zhang, Y.; He, S.; Guo, W.; Hu, Y.; Huang, J.; Mulcahy, J. R.; Wei, W. D. Surface-Plasmon-Driven Hot Electron Photochemistry. *Chem. Rev.* **2018**, *118* (6), 2927–2954. https://doi.org/10.1021/acs.chemrev.7b00430.

(26) Brown, A. M.; Sundararaman, R.; Narang, P.; Goddard III, W. A.; Atwater, H. A. Nonradiative Plasmon Decay and Hot Carrier Dynamics: Effects of Phonons, Surfaces, and Geometry. *ACS Nano* **2016**, *10*, 957–966. https://doi.org/10.1021/acsnano.5b06199.

(27) Bard, A. J. Inner-Sphere Heterogeneous Electrode Reactions. Electrocatalysis and Photocatalysis: The Challenge. *J. Am. Chem. Soc.* **2010**, *132* (22), 7559–7567. https://doi.org/10.1021/ja101578m.

(28) Bard, A. J.; Faulkner, L. R. *Electrochemical Methods: Fundamentals and Applications*, 2nd Editio.; Wiley, Ed.; New York, 2001.

(29) Henrotte, O.; Boudet, A.; Limani, N.; Bergonzo, P.; Zribi, B.; Scorsone, E.; Jousselme, B.; Cornut, R. Steady-State Electrocatalytic Activity Evaluation with the Redox Competition Mode of Scanning Electrochemical Microscopy : A Gold Probe and a Boron-Doped Diamond Substrate. *ChemElectroChem* **2020**, *7*, 4633–4640. https://doi.org/10.1002/celc.202001088.

(30) Ingram, D. B.; Linic, S. Water Splitting on Composite Plasmonic-Metal/Semiconductor Photoelectrodes : Evidence for Selective Plasmon-Induced Formation of Charge Carriers

near the Semiconductor Surface. *J. Am. Chem. Soc.* **2011**, *133*, 5202–5205.

(31) Liu, Z.; Hou, W.; Pavaskar, P.; Aykol, M.; Cronin, S. B. Plasmon Resonant Enhancement of Photocatalytic Water Splitting Under Visible Illumination. *Nano Lett.* **2011**, *11* (3), 1111–1116. https://doi.org/10.1021/nl104005n.

(32) Bian, Z.; Tachikawa, T.; Zhang, P.; Fujitsuka, M.; Majima, T. Au/TiO2 Superstructure-Based Plasmonic Photocatalysts Exhibiting Efficient Charge Separation and Unprecedented Activity. *J. Am. Chem. Soc.* **2014**, *136* (1), 458–465. https://doi.org/10.1021/ja410994f.

(33) Kumaravel, V.; Mathew, S.; Bartlett, J.; Pillai, S. C. Photocatalytic Hydrogen Production Using Metal Doped TiO2: A Review of Recent Advances. *Appl. Catal. B Environ.* **2019**, *244*, 1021–1064. https://doi.org/10.1016/j.apcatb.2018.11.080.

(34) Wang, S.; Gao, Y.; Miao, S.; Liu, T.; Mu, L.; Li, R.; Fan, F.; Li, C. Positioning the Water Oxidation Reaction Sites in Plasmonic Photocatalysts. *J. Am. Chem. Soc.* **2017**, *139* (34), 11771–11778. https://doi.org/10.1021/jacs.7b04470.

(35) Zhang, J.; Jin, X.; Morales-guzman, P. I.; Yu, X.; Liu, H.; Zhang, H.; Razzari, L.; Claverie, J. P. Engineering the Absorption and Field Enhancement Properties of Au−TiO2 Nanohybrids via Whispering Gallery Mode Resonances for Photocatalytic Water Splitting. *ACS Nano* **2016**, *10*, 4496–4503. https://doi.org/10.1021/acsnano.6b00263.

(36) Link, S.; El-Sayed, M. A. Size and Temperature Dependence of the Plasmon Absorption of Colloidal Gold Nanoparticles. *J. Phys. Chem. B* **1999**, *103* (21), 4212–4217. https://doi.org/10.1021/jp984796o.

(37) Jain, P. K.; Lee, K. S.; El-Sayed, I. H.; El-Sayed, M. A. Calculated Absorption and Scattering Properties of Gold Nanoparticles of Different Size, Shape, and Composition:

Applications in Biological Imaging and Biomedicine. *J. Phys. Chem. B* **2006**, *110* (14), 7238–7248. https://doi.org/10.1021/jp057170o.

(38) Ratchford, D. C.; Dunkelberger, A. D.; Vurgaftman, I.; Owrutsky, J. C.; Pehrsson, P. E. Quantification of Efficient Plasmonic Hot-Electron Injection in Gold Nanoparticle-TiO2 Films. *Nano Lett.* **2017**, *17* (10), 6047–6055. https://doi.org/10.1021/acs.nanolett.7b02366.

(39) Yu, Y.; Sundaresan, V.; Willets, K. A. Hot Carriers versus Thermal Effects: Resolving the Enhancement Mechanisms for Plasmon-Mediated Photoelectrochemical Reactions. *J. Phys. Chem. C* **2018**, *122* (9), 5040–5048. https://doi.org/10.1021/acs.jpcc.7b12080.

(40) Sanchez-Sanchez, C. M.; Rodriguez-Lopez, J.; Bard, A. J. Scanning Electrochemical Microscopy. 60. Quantitative Calibration of the SECM Substrate Generation / Tip Collection Mode and Its Use for the Study of the Oxygen Reduction Mechanism. *Anal. Chem.* **2008**, *80* (9), 3254–3260.

(41) Khurgin, J. B. Fundamental Limits of Hot Carrier Injection from Metal in Nanoplasmonics. *Nanophotonics* **2020**, *9* (2), 453–471.

(42) Naldoni, A.; Guler, U.; Wang, Z.; Marelli, M.; Malara, F.; Meng, X.; Besteiro, L. V; Govorov, A. O.; Kildishev, A. V; Boltasseva, A.; Shalaev, V. M. Broadband Hot-Electron Collection for Solar Water Splitting with Plasmonic Titanium Nitride. *Adv. Opt. Mater.* **2017**, *5*, 1601031. https://doi.org/10.1002/adom.201601031.

(43) Santiago, E. Y.; Besteiro, L. V; Kong, X.; Correa-duarte, M. A.; Wang, Z.; Govorov, A. O. Efficiency of Hot-Electron Generation in Plasmonic Nanocrystals with Complex Shapes: Surface-Induced Scattering, Hot Spots, and Interband Transitions. *ACS Photonics* **2020**, *7*, 2807–2824. https://doi.org/10.1021/acsphotonics.0c01065.

(44) Movsesyan, A.; Santiago, E. Y.; Burger, S.; Correa-duarte, M. A.; Besteiro, L. V; Wang, Z.; Govorov, A. O. Plasmonic Nanocrystals with Complex Shapes for Photocatalysis and Growth : Contrasting Anisotropic Hot-Electron Generation with the Photothermal Effect. *Adv. Opt. Mater.* **2022**, *10*, 2102663. https://doi.org/10.1002/adom.202102663.

(45) Varghese, O. K.; Paulose, M.; Grimes, C. A. Long Vertically Aligned Titania Nanotubes on Transparent Conducting Oxide for Highly Efficient Solar Cells. *Nat. Nanotechnol.* **2009**, *4* (9), 592–597. https://doi.org/10.1038/nnano.2009.226.

(46) Villanueva-Cab, J.; Jang, S.-R.; Halverson, A. F.; Zhu, K.; Frank, A. J. Trap-Free Transport in Ordered and Disordered TiO2 Nanostructures. *Nano Lett.* **2014**, *14*, 2305–2309.

(47) Cha, G.; Schmuki, P.; Altomare, M. Anodic TiO2 Nanotube Membranes : Site-Selective Pt-Activation and Photocatalytic H2 Evolution. *Electrochim. Acta* **2017**, *258*, 302–310. https://doi.org/10.1016/j.electacta.2017.11.030.

(48) Lefrou, C.; Cornut, R. Analytical Expressions for Quantitative Scanning Electrochemical Microscopy (SECM). *ChemPhysChem* **2010**, *11* (3), 547–556. https://doi.org/10.1002/cphc.200900600.

(49) Baur, J. E. 19 - Diffusion Coefficients. In *Handbook of electrochemistry*; Zoski, C. G., Ed.; Elsevier: Amsterdam, 2007; pp 829–848. https://doi.org/https://doi.org/10.1016/B978-044451958-0.50036-7.

For Table of Contents Only